

# Automated Structural-level Alignment of Multi-view TLS and ALS Point Clouds in Forestry

Juan Castorena<sup>a</sup>, L. Turin Dickman<sup>a</sup>, Adam J. Killebrew<sup>a</sup>, James R Gattiker<sup>a</sup>, Rod Linn<sup>a</sup>, E. Louise Loudermilk<sup>b</sup>

<sup>a</sup>*Los Alamos National Laboratory, Los Alamos, NM, 48124 USA*

<sup>b</sup>*Southern Research Station, 200 W.T. Weaver Blvd. Asheville, NC 28804-3454, USA*

---

## Abstract

Access to highly detailed models of heterogeneous forests from the near surface to above the tree canopy at varying scales is of increasing demand as it enables more advanced computational tools for analysis, planning, and ecosystem management. LiDAR sensors available through different scanning platforms including terrestrial, mobile and aerial have become established as one of the primary technologies for forest mapping due to their inherited capability to collect direct, precise and rapid 3D information of a scene. However, their scalability to large forest areas is highly dependent upon use of effective and efficient methods of co-registration of multiple scan sources. Surprisingly, work in forestry in GPS denied areas has mostly resorted to methods of co-registration that use reference based targets (e.g., reflective, marked trees), a process far from scalable in practice. In this work, we propose an effective, targetless and fully automatic method based on an incremental co-registration strategy matching and grouping points according to levels of structural complexity. Empirical evidence shows the method's effectiveness in aligning both TLS-to-TLS and TLS-to-ALS scans under a variety of ecosystem conditions including pre/post fire treatment effects, of interest to forest inventory surveyors.

**Keywords:** Registration, LiDAR, Point Cloud, ALS, TLS, Automatic, Forest

---

## 1. Introduction

Forests cover approximately four billion hectares amounting to roughly 31% of the earth's land area [1]. Demand for tools that help maintain the balance of a healthy forest ecosystem are increasing but their complexity is challenging as it depends on a wide range of factors including resilience against disease and fire, health and biodiversity [2]. Methods that help collect information about these factors and that consider the heterogeneity of the forest and its changes over time is an active area of research seeking to provide the means for improved planning, management, analysis and more effective and efficient decision-making [3]. Traditionally, one of the most widely used tools for measurement are national forest inventory (NFI) plots that use spatial sampling and estimation techniques to quantify factors including forest cover, growing stock volume, biomass, carbon balance and tree measurements (e.g., diameter at breast height, crown width, height) [4]. Limitations are however, that these plots are typically field sampled by hand, which can be economically costly and time consuming especially when considering large spatial scales extents (e.g., 1 million ha).

Remote sensing techniques including terrestrial laser scanning (TLS), aerial laser scanning (ALS) and optical photogrammetry have been established as technologies offering time and cost economies at scale [2] in forest surveys. From these, LiDAR based scanning has gained widespread interest due to its inherent capabilities to directly collect precise 3D structural information very rapidly and over large regional extents [5]. Airborne based LiDAR for example, utilizing accurate position sensors including RTK, enables large scale mapping at spatial resolutions in the order of  $\sim 10$  pts/m<sup>2</sup>. It has shown to be effective in retrieving factors of interest in forest inventory plots [6], however, some limitations exist as it has problems penetrating the tree canopy cover in dense areas even with its powerful but computationally demanding full-waveform based technology. TLS, on the other hand [7], is complementary to ALS as it is capable of collecting 3D maps at much higher spatial resolutions providing detailed 3D information about individual trees, shrubs, ground surface and near ground vegetation. However, strategies and methods for moving the scanning system and fusing their data from multiple scans to increase the field of view can be challenging. The

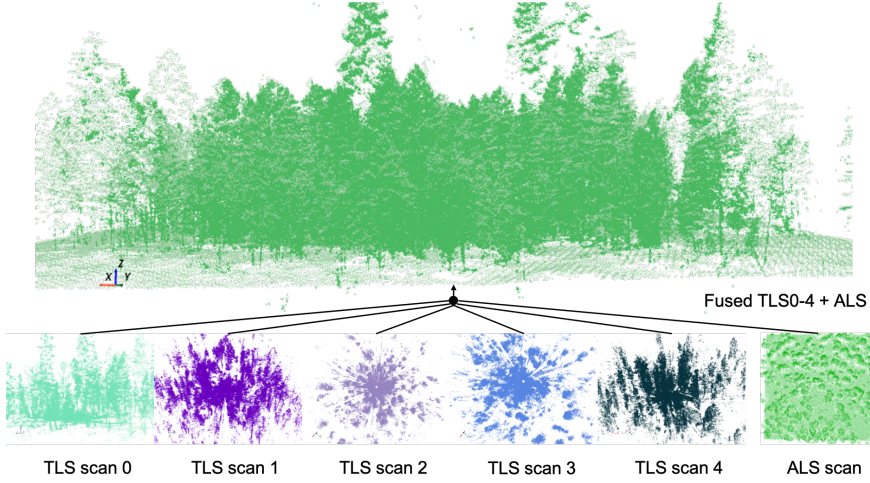


Figure 1: Alignment of 5 multi-view TLS and ALS in forest.

simplest of strategies consists of placing the scanner at different locations within a plot (i.e., multi-view TLS), but other more sophisticated options exist including hand-held scanners [8]. Having access to a diversity of sources can offer the enhanced capabilities of all: enabling precise, 3D information from the near surface vegetation to the top of the canopy at scale; a characteristic rarely available when a single scanning mode is used [7]. Here, we focus our scope on one of the fundamental enablers for combining scanning sources in forest ecosystems: co-registration or alignment approaches allowing projection of multi-source data into a common, consistent coordinate system.

Most studies that establish the complementary nature between multi-view TLS and ALS in forestry [9, 8, 10, 11, 12] have utilized known physically placed reference targets (e.g., multiple uniform size spheres, retro-reflective targets), which are detected and matched between scans for alignment. Unfortunately, this group of target based methods tends to render LiDAR data collection less scalable and more time consuming. In contrast, targetless methods in forestry [13, 14, 15, 16, 17, 18] have used extracted tree features (e.g., stem size, stem axis, breast height, distances between trees) for finding alignment correspondences. These methods tend, however, to be sensitive to the accuracy of the tree extraction method; a process that can become computationally demanding in dense forest areas and prone to significant errors. Other alternatives have resorted to position sensors including GNSS/IMU systems in multi-view TLS in forestry settings [8], but have found inferior performances due to higher uncertainties or missing measurements in areas of poor or nonexistent satellite based georeferencing [19].

Within the fields of computer vision and robotics, many automatic and targetless point cloud registration methods exist. Examples include the seminal iterative closest point (ICP) [20], point-to-plane ICP [21], 4 point co-planar sets [22], feature point feature histograms (FPFH) [23] and more recent learning based methods [24, 25]. These methods do not require a target and use rule or learned based features within the scene to find correspondences. Applications involving point clouds from shaped objects and urban scenes have been very successful for registration using these approaches. However, such methods typically assume a highly structured environment and suffer when applied in a straightforward manner in complex heterogeneous forest environments. The presence of non-uniform structures such as bushes, leaves, bark, branches on the forest surface, dense and heterogeneous tree types, and the non-uniformity of the forest surface can make standard registration methods highly prone to miss-alignment. In addition, partial (i.e., existing only in a limited region), as opposed to sparse or full overlap, is also problematic for most conventional 3D registration approaches. This is often the case in forests, where both sensor ranges and distances between scan centers and occlusion in densely populated forests from vegetation or steep terrain may have a significant effect.

In light of these limitations, we propose a new method based on a notion of structural complexity: a metric encoding information about point distribution. Here, we use this metric to group and match point subsets later used in an incremental fashion until full-scan alignment. We show, this grouping and matching of scan point subsets based on structural complexity is an effective strategy for co-registering scans from highly complex and heterogeneous forest environments under a variety of conditions of interest to forest managers. Figure 1 illustrates an example result for the

refined alignment of five color-coded multi-view TLS scans from a New Mexico, USA forest ecosystem. Advantages of the proposed method are its effectiveness in registering LiDAR scans in complex forest environments, while not requiring position sensors, reference human placed targets, extraction of trees or other semantic features, and is fully automatic. Section 3 describes our approach more in detail while Section 4 shows the overall performance of our method along with a few illustrative examples. Finally, Section 5 summarizes our contributions and findings.

## 2. Related works

Here, we summarize relevant prior art developed to co-register multiview TLS and ALS. On TLS-to-TLS, several works have been proposed. In urban scenarios for example, the work of [26] approximated scenes by planar patches and used them as features to globally optimize the alignment parameters. [27] projected 3D points into a ground occupancy 2D plane image and based its registration approach in aligning these occupancy planes. Along a similar principle, [28] proposed a birds eye view 3D-to-2D point cloud projection method and used SIFT features to register scan pairs. These set of methods however, were designed to register highly structured urban environments containing buildings, houses and man-made structures and do not work well in cases where the scene does not contain sharp edges, corners or planar like shapes. Instead, the work of [29] specifically focused on registering TLS scans from forest environments. It relies on semantic segmentation of tree stem and branch centers of scans containing a single tree. Extensions to registering scans with more trees is however not straightforward while also being dependent upon the accuracy of the semantic segmentation stage.

On the TLS-to-ALS side, the story is similar; most works rely on using features suitable to urban scenarios and are thus not applicable to natural environments. The work of [30] for example, used wavelets to detect edges in buildings and later matched these in between TLS and ALS for registration. [31] instead registered scans by extracting and matching planar like structures while [32] used both edges and planes to register scans containing buildings. The works of [33, 34, 35] extracts urban building outlines/contours/boundaries and is thus dependent on the regularity of corners, edges and planes for this purpose. But as in all the aforementioned methods, these works focus on registering urban scenes and their fundamental step of feature extraction/correspondence is not suitable for natural scenery. Efforts In [16, 17, 36, 37, 38] proposed methods to register LiDAR scans coming from forest environments by finding relative tree feature distances. The efficacy of these methods however, is dependent upon the accuracy of the tree segmentation step which tends to degrade as a function of increasing tree density.

## 3. Approach

Co-registration of multiple LiDAR point cloud sources seeks to align and stitch/accumulate all scan sources into a global or common and consistent coordinate system. Scan sources can come from multi-view perspectives, from different sensors, and/or a variety of scanning platforms (static TLS, mobile TLS, UAV's, ALS). As we are focusing on methods that are both automatic, targetless and without the use of position and orientation sensing, we restrict our approach to scan sources that have at least partial overlap. This section describes the proposed alignment method mainly consisting of two stages: (1) an incremental multi-structural complexity registration between scan pairs and (2) a bundle refinement distributing errors between multiple scan views. To the best of our knowledge, this is the first fully automatic and targetless based method capable of registering both TLS-to-TLS and TLS-to-ALS scans under a variety of Forest ecosystem conditions and that does not depend on the accuracy of any prior semantic segmentation approach (e.g., tree segmentation).

In terms of notation, a LiDAR scan is denoted by  $\mathbf{X} \in \mathbb{R}^{N \times 3}$  with  $N$  being the number of points in the scan and 3 being the point coordinates in the  $x$ ,  $y$  and  $z$ -axes. A subscript  $s$  or  $t$  attached to the right of  $\mathbf{X}$  is used to distinguish between a source  $s$  and a target  $t$  scan while a superscript  $i$  as in  $\mathbf{X}^{(i)}$  denotes a selection of point(s) according to index or index set  $i$ . For a pair of scans, registration is characterized by an aligning rigid body transformation consisting of 6 orientation/position degrees of freedom (DOF): three rotation angles ( $\theta_{\text{roll}}$ ,  $\theta_{\text{pitch}}$ ,  $\theta_{\text{yaw}}$ ) and three translations ( $t_x$ ,  $t_y$ ,  $t_z$ ). 3D Rotations are represented by the matrix  $\mathbf{R} \in \mathbf{SO}(3)$  in the special orthogonal group  $\mathbf{SO}(3)$  while translations are equivalently denoted as the vector  $\mathbf{t} \in \mathbb{R}^3$  of  $t_x$ ,  $t_y$ ,  $t_z$  coordinate elements. The subscript and superscripts attached on the right of  $\mathbf{R}$ ,  $\mathbf{t}$  denotes that this transformation takes from the coordinate system of the subscript, to that of the superscript while the subscript  $m$  attached to the left of  $\mathbf{R}$ ,  $\mathbf{t}$  denotes the  $m$ -th index.

### 3.1. Pair-wise registration

The core idea of the proposed pair-wise registration approach is to align pairs of scans by incrementally aligning matching groups of point subsets grouped and matched by structural complexity similarities. Rather than using standard human engineered or learned features, we make use of a notion of structural complexity to establish similarity. This, different from standard methods relying on features characteristic of human made objects or scenes (e.g., corners, edges, planar facets, contours, spheres, etc.) which rarely appear in complex heterogeneous forests, or from semantic segmentation based methods (e.g., trees) requiring accurate estimates. Structural complexity here, is a metric encoding information uncertainty in point range distributions at relative height point-to-plane projections. Similarities are assessed by computing the uncertainty in conditional point range distributions. These metrics are meant as a quick method for comparisons, group and match sets of points as it only involves low-level operations without the need of detection of calibration targets, nor object segmentation. The mathematical descriptions of structural complexity (SC) and similarity (SS) utilized here are based on entropy and mutual information (MI) [39] measures from information theory. Here, these quantities are measured by:

$$SC(q, k) = \sum_{\mathbf{X}_q^{(j_q^k)}} p\left(r_{\phi, k\Delta z}(\mathbf{X}_q^{(j_q^k)}) | h_{\phi, k\Delta z}(\mathbf{X}_q) = j_q^k\right) \log p\left(r_{\phi, k\Delta z}(\mathbf{X}_q^{(j_q^k)}) | h_{\phi, k\Delta z}(\mathbf{X}_q) = j_q^k\right) \quad (1)$$

where  $r_{\phi, k\Delta z} : \mathbb{R}^{N \times 3} \rightarrow \mathbb{R}^{N \times 1}$  is a function computing the range of point-to-plane projections parameterized by plane parameters  $\phi$  at height  $k\Delta z$  while  $h_{\phi, k\Delta z} : \mathbb{R}^{N \times 3} \rightarrow \mathbb{R}^{N \times 1}$  returns point indices bounded a distance away from the point-to-plane projection. SS is given as:

$$SS(i^{l_s}, i^{l_t}) = \sum_{\mathbf{X}_s^{(i^{l_s})}} \sum_{\mathbf{X}_t^{(i^{l_t})}} p\left(r_{\phi, k\Delta z}(\mathbf{X}_s^{(i^{l_s})}), r_{\phi, k\Delta z}(\mathbf{X}_t^{(i^{l_t})})\right) \log \frac{p\left(r_{\phi, k\Delta z}(\mathbf{X}_s^{(i^{l_s})}), r_{\phi, k\Delta z}(\mathbf{X}_t^{(i^{l_t})})\right)}{p\left(r_{\phi, k\Delta z}(\mathbf{X}_s^{(i^{l_s})})\right) p\left(r_{\phi, k\Delta z}(\mathbf{X}_t^{(i^{l_t})})\right)}. \quad (2)$$

Eq.(2) computes SS over point range distributions which encode structural complexities. The MI principle behind Eq.(2) has been shown to be effective in registering multiple modalities (e.g., LiDAR and camera) [40] as an optimization metric, but here we use it only to group and match point subsets intra/inter-scan. Similarly, point-to-plane projections have been used before for registering LiDAR scans as a feature compression mechanism. Here, however, we do not use projected points as features for registration as in [33, 34, 27, 35, 28], but rather for grouping points and finding correspondences between groups. Also, the sliding point-to-plane projection strategy is different from previous works that only use a single bird's eye view as features [33, 34]. Furthermore, notions of structural scene complexity have been used previously in [41, 42], but therein used to sub-sample scenes at varying complexity based on the waveform envelope shape in full-waveform LiDAR.

**Grouping and Matching** is an algorithm developed here to group and match point subsets by structural similarity. It encompasses two tasks: (1) Intra-scan groupings, conglomerating point subsets of a scan into levels of structural similarity and (2) Inter-scan matching, encompassing matching structurally similar levels between pairs of source and target scans. Intra-scan point group subsets are formed by sequentially sliding a plane in the direction of a plane's normal and associating in a set of indices  $j_q^k$  for sliding plane index  $k \in \{1, \dots, K\}$  and scan  $q \in \{s, t\}$  points which are at most a normal distance  $\Delta h t$  away. The sliding plane starts at the ground of the scan (i.e.,  $k = 0$ ) and moved up at uniform shifts  $\Delta z$  until  $K$ . An illustration of this is included in Figure 2 showing a tree from two distinct scan views. The range of each point in the  $x, y$  direction relative to the plane's axis center is then computed though a point-to-plane projection used to obtain a histogram representing point range distribution. Point range distributions across sliding planes  $\phi, k\Delta z$  are compared to find structural similarities between them and those found similar are organized into groups each representing a complexity level. The number of groups representing complexity can vary depending on the scene but throughout all experiments here we set this to three for each scan. The plane closest to the sensor's coordinate axis is extracted by fitting a 3D plane using the random sampling and consensus (RANSAC) algorithm [43] assuming the ground surface can be approximated at least in the vicinity of the LiDAR scan's center by a plane in some random orientation.

Inter-scan matching seeks to find correspondences in structural complexity levels between the scans. Matchings are posed as an assignment problem with a one-to-one correspondence between the formed groups in the source and

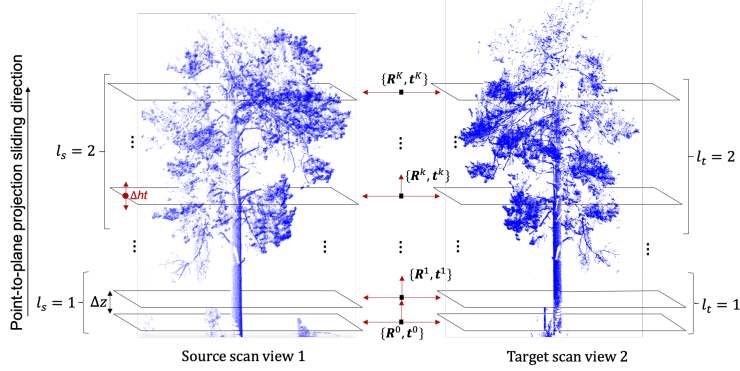


Figure 2: Multilevel registration of example scans.

target scans. This problem is formulated here as the bijective matching that maximizes the sum of pair-wise structural similarities:

$$\hat{\mathbf{A}} = \arg \max \sum_{l_s} \sum_{l_t} A_{l_s, l_t} I(\mathbf{X}^{i_s}, \mathbf{X}^{i_t}) \quad (3)$$

subject to the constraints that  $A_{l_s, l_t} \in \{0, 1\}$  and  $\sum_{l_s} A_{l_s, l_t} = 1$ ,  $\sum_{l_t} A_{l_s, l_t} = 1$ ,  $\forall l_s, l_t$ . This problem has been formulated before in the context of computing 3D LiDAR point flows in [44] but here to match structural level similarities between scans. Solutions to this problem exist in [45]. For compactness, we represent the estimate  $\hat{\mathbf{A}}$  through the matched indices function between source levels  $l_s \in \{1, \dots, L\}$  and target level  $l_t \in \{1, \dots, L\}$  as  $l_t = \sigma(l_s)$  where the support of  $\sigma : \mathbb{Z} \rightarrow \mathbb{Z}$  is denoted as  $L = |\sigma|$ . One additional note is that the structural similarities in Eq.(3), are computed through point range distributions with the point-to-plane projection that best fits the grouped points in each scan.

The incremental property of the proposed approach provides the capability to improve alignment estimates over time and inherits its ability to recover from bad initial or first iterate estimates. Grouped points are registered starting from the corresponding levels of lower structural complexity and moving up into the more complex. Level complexity is measured by Eq.(1) using the point indices of  $i_s^{l_s}$ . At each matched structural level ICP is used only at the points indexed by  $i_s^{l_s}$  and the matched  $i_t^{\sigma(l_s)}$  for the specific level  $l_s$ . The resulting transformation  $\{\mathbf{R}^{l_s}, \mathbf{t}^{l_s}\}$  is subsequently used as initialization at the next complexity level and so forth, thus its incremental nature, until a pre-defined level  $L$  is reached ( $L=3$  in all experiments here). One thing to note here is that the indexed point cloud at each structural level is downsampled (denoted as a  $\downarrow_{\delta_{l_s}}$  attached next to a scan  $\mathbf{X}$ ) using a uniform grid of cell size  $\delta_{l_s}$  to reduce differences in point densities between scans and to minimize the registration bias effect of areas that are more densely sampled due to the sensor's scanning nature (e.g., from proximity: objects near the sensor in TLS or canopy in ALS). Moreover, this downsampling also reduces the computational demands of running ICP on densely sampled scan pairs. Here, we use the downsampling constant factor function with step size  $\delta_0 = 0.25$  (m.) throughout all levels, but others can be used depending on the scanning density characteristic of the sensor. In a last step, ICP is re-run on the entire point cloud using as initialization the last computed estimates  $\{\mathbf{R}^L, \mathbf{t}^L\}$  and just for a few iterates (e.g., 50) with a finer downsampling resolution (e.g.,  $\delta = 0.025$  (m.)). A summary of the whole described co-registration approach is included in Algorithm 1 and a schematic example is shown in Fig. 2.

### 3.2. Bundle refinement

In bundle refinement, small errors resulting from pair-wise alignments are treated through bundle refinements to prevent error propagation in the presence of multiple scans. This error is reduced by incorporating cycle consistency constraints between the multiple scans. The set of  $C$  scan sources are represented by a graph where each node is the center of each scan source  $\mathbf{c}_i$  for  $i \in \{0, \dots, C\}$  in the common/global coordinate system and edges are just artificial connections between any pair of nodes. The relative positions of scan node  $\mathbf{c}_1$  to  $\mathbf{c}_0$  connected by an edge can be expressed as in Eq.(4):

$$\mathbf{R}_{\mathbf{c}_1}^{\mathbf{c}_0} = \mathbf{R}_w^{\mathbf{c}_0} \mathbf{R}_{\mathbf{c}_1}^w, \quad \mathbf{t}_{\mathbf{c}_1}^{\mathbf{c}_0} = \mathbf{R}_w^{\mathbf{c}_0} (\mathbf{t}_{\mathbf{c}_0}^w - \mathbf{t}_{\mathbf{c}_1}^w) \quad (4)$$

---

**Algorithm 1** Pair-wise multi-level registration

---

```

1: Input: Source  $\mathbf{X}_s$  and target  $\mathbf{X}_t$  point clouds.
2: Set: downsampling factors  $\delta_0 = 0.25(\text{m})$ ,  $\delta = 0.025(\text{m})$ ,  $\Delta ht = 0.25(\text{m})$ , plane shifts  $K = \frac{\max \text{height}}{\Delta ht}$ , structural groups  $L = 3$ 
3:     Initializations  $\mathbf{R}^0, \mathbf{t}^0$ .
4: Intra-scan groupings:
5:     for  $q$  in  $\{s, t\}$  do:
6:         Downsample point clouds  $\tilde{\mathbf{X}}_q = \mathbf{X}_q \downarrow_{\delta_0}$ 
7:         Get most dominant plane  $\mathbf{p}_q = \text{RANSAC}\{\tilde{\mathbf{X}}_q\}$ 
8:         for  $k$  in  $[0, \dots, K]$  do:
9:             // Extract points bounded a distance away from point-to-plane projection
10:              $j_q^k = \{i : \mathbf{p}_q \tilde{\mathbf{X}}_q^i \geq (k-1) \cdot \Delta ht \quad \& \quad \mathbf{p}_q \tilde{\mathbf{X}}_q^i < k \cdot \Delta ht \quad \forall i\}$ 
11:         end
12:         // Group point indices by structural similarities using  $k$ -means.
13:          $\ell_q = k\text{-means}([\text{SC}(q, 0), \text{SC}(q, 1), \dots, \text{SC}(q, K)], L)$    with    $\ell_q = \cup_{l=1}^L \ell_q^l = \{0, 1, \dots, K\}$ 
14:          $i_q^l = \{j_q^k : k \in \ell_q^l\}$ 
15:     end
16:     Output: Structural complexity point level indices  $\{i_s^l, i_t^l\}$ 
17: Inter-scan level matchings:
18:     Use  $\text{SC}(i_s^l, i_t^l)$  in Eq. (3) and compute  $\sigma$  with  $L = |\sigma|$ 
19: Incremental registration:
20:     for  $l$  in  $[0, \dots, L]$  do:
21:          $\{\mathbf{R}^l, \mathbf{t}^l\} = \text{ICP}(\tilde{\mathbf{X}}_s^{i_s^l}, \tilde{\mathbf{X}}_t^{i_t^l}, \{\mathbf{R}^{l-1}, \mathbf{t}^{l-1}\})$ 
22:     end
23:     run:  $\{\mathbf{R}, \mathbf{t}\} = \text{ICP}(\mathbf{X}_s \downarrow \delta, \mathbf{X}_t \downarrow \delta, \{\mathbf{R}^L, \mathbf{t}^L\})$ 
24: Output: Rotation and translation  $\{\mathbf{R}, \mathbf{t}\}$ .

```

---

where  $w$  represents a world coordinate system. Refinement is achieved by imposing a cycle consistency constraint between all paths connecting node  $\mathbf{c}_1$  to node  $\mathbf{c}_0$ . Here, a path in a graph is any sequence of edges connecting at least any two nodes. For ease of exposition Fig.3 illustrates this with a graph of five node scans. Non-exhaustive example paths between  $\mathbf{c}_1, \mathbf{c}_0$  in this case include:  $\mathbf{c}_1 \rightarrow \mathbf{c}_0$ ,  $\mathbf{c}_1 \rightarrow \mathbf{c}_2 \rightarrow \mathbf{c}_0$ ,  $\mathbf{c}_1 \rightarrow \mathbf{c}_3 \rightarrow \mathbf{c}_0$ ,  $\mathbf{c}_1 \rightarrow \mathbf{c}_4 \rightarrow \mathbf{c}_0$ ,  $\mathbf{c}_1 \rightarrow \mathbf{c}_3 \rightarrow \mathbf{c}_4 \rightarrow \mathbf{c}_2 \rightarrow \mathbf{c}_0$ . Similar to Eq.(4), the relative position between nodes  $c_i$  to  $c_j$  through a path  $m$  composed

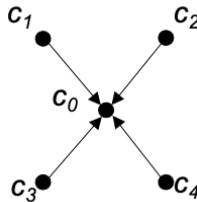


Figure 3: A graph with five nodes.

of  $N^m$  nodes indexed by  $n$  (abusing notation as  $n$  is assumed to respect the sequence order of nodes in the path), can be obtained as in Eq.(5):

$${}_m \mathbf{R}_{\mathbf{c}_i}^{\mathbf{c}_j} = \prod_{n=i}^j \mathbf{R}_{\mathbf{c}_n}^{\mathbf{c}_{n+1}}, \quad {}_m \mathbf{t}_{\mathbf{c}_i}^{\mathbf{c}_j} = \sum_{n=i}^j {}_n \mathbf{t}_{\mathbf{c}_n}^{\mathbf{c}_{n+1}} \quad (5)$$

Here, the set of paths is of cardinality  $M$  and  $m$  is an index of a specific path. Imposing cycle consistency throughout all LiDAR scan sources thus consists in minimizing at each node  $\mathbf{c}_i$  the estimation errors from a set of paths. This can

be formulated as the computation of the rotation and translation at  $\mathbf{c}_i$  that minimizes the sum of distances in Eq.(6):

$$\hat{\mathbf{R}}_{\mathbf{c}_i}^w = \arg \min_{\mathbf{R} \in \mathbf{SO}(3)} \left\{ \sum_{m=1}^M \|\log(\mathbf{R}^T m \mathbf{R}_{\mathbf{c}_i}^w)\| \right\}, \quad \hat{\mathbf{t}}_{\mathbf{c}_i}^w = \arg \min_{\mathbf{t} \in \mathbb{R}^3} \left\{ \sum_{m=1}^M \|_m \mathbf{t}_{\mathbf{c}_i}^w - \mathbf{t} \|_{\ell_2} \right\} \quad (6)$$

where  $\|\log(\mathbf{R}^T m \mathbf{R}_{\mathbf{c}_i}^w)\|$  is the Riemannian distance measuring the shortest geodesic between rotations and the second rotation term can be obtained as  $_m \mathbf{R}_{\mathbf{c}_i}^w = \mathbf{R}_{\mathbf{c}_i}^w m \mathbf{R}_{\mathbf{c}_i}^w$ . The intuition behind the problem in Eq.(6) is simple; in general, we find the rotation  $\mathbf{R} \in \mathbf{SO}(3)$  that minimizes the Euclidean distance between the vector of unit energy rotated by  $\mathbf{R}$  and a set of rotated sampled vector estimates each also of unit energy. Finding the parameters that optimally solve Eq.(6) relative to the rotations  $\mathbf{R}$  can be done using either the  $\ell_2$  average of rotations [46] computed by the exponential gradient descent or the more robust to outliers  $\ell_1$  average computed with the Weiszfeld algorithm [47]. Solving Eq.(6) for the translation can be done by computing a  $\mathbf{t}$  at which the gradient of its cost is equal to zero which corresponds to the translation average.

## 4. Experiments

In the following set of experiments we validate our approach in several case scenarios: pair-wise and multi-view registration. Validation is performed on real LiDAR point cloud datasets: (1) on multi-view TLS scans (2) on collocated TLS and ALS. Datasets were collected from a variety of forest ecosystems with most within the boundaries of the Bandelier National Monument in New Mexico, USA in high elevation mixed-conifer forest, unless otherwise specified. Implementations were performed in Python, with the VTK based PyVista module visualizer and using some tools from Open3d [48], in particular ICP and downsampling functionality.

### 4.1. Datasets

The TLS dataset was collected in the summer of 2022 using a Leica BLK360 LiDAR with a laser scanner operating at a 830 nm wavelength and fields of view (FOV) of 300° and 360° in the vertical and horizontal directions, respectively. The LiDAR was mounted in a static tripod while scanning. The center locations of forest inventory plots (FIP) were used as reference for positioning a "center" LiDAR scan while multi-view scans were placed within the FIP quadrants that altogether define the FIP area coverage. A total of 21 plots were LiDAR surveyed and used each with five multi-view scans per plot. The inventory plots were 50 x 20 (m) and the LiDAR scans were positioned one at the center while the other four distributed  $\sim 15 \times 5$  meters apart from the center in each of the four corners similar to as shown in Fig. 3. An example of the distribution of points resulting from a single scan with a mostly flat ground surface is included in Figure 4.(a). Approximately 8 million points were measured per scan with 4.6 million reflected from the ground. Most of the returns are concentrated below the 15 (m) range in general, while most returns are below 10(m) for the ground surface.

The ALS data was collected in October 2021 by TetraTech over 170 square miles around Los Alamos, NM. The ALS system included a Galaxy T2000 LiDAR sensor mounted on a fixed-wing aircraft. The LiDAR operates with a 1064 nm wavelength laser and is capable of collecting up to 8 multiple returns per laser fired. The scan FOV of this LiDAR is 10-60° with an accuracy of <0.03-0.25 m RMSE within the 150-6500 m range. The surveyed area was completed in 55 flight lines, including 7 cross strips to ensure a point density of 10 points per square meter. Note that the ALS datasets utilized here all include the 8 multiple returns per laser fired which increases the density of point returns from below the canopy. Since there is no occlusion for satellite signals in ALS, its scans were aligned with a Trimble CenterPoint RTX positioning system that delivers accuracies at the centimeter (cm) level.

*Performance Metrics:* All our quantitative evaluations were performed using the registration root mean square error (RMSE) metric. Here, registration RMSE was measured relative to the ground truth six degrees of freedom orientation and position registration parameters. Ground truth was obtained by running our approach on TLS ground scans for 10 trials on each pair-wise scan, averaging registration parameters and checking for consistency with augmented ALS. Consistency with ALS was verified by comparing with the relative orientations and positions found by localizing the TLS scan centers projected into the ground plane in ALS and finding the orientation and translations relative to each scan. The validated parameters were used as ground truth, noticing that RTX aligned ALS provides accuracies within the centimeter level. Overlap is measured as % of points in source having at least a correspondence

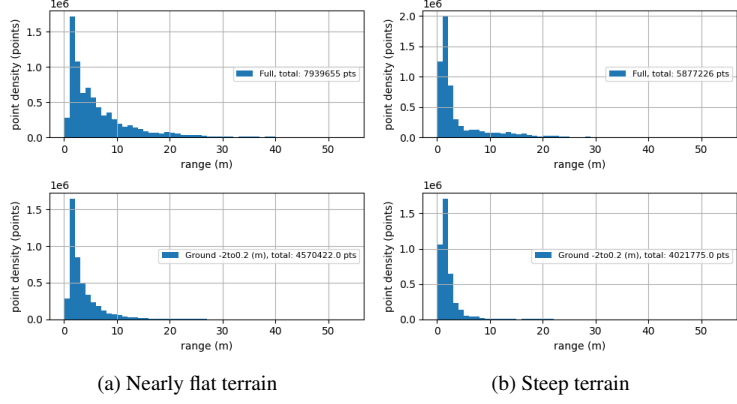


Figure 4: BLK360 LiDAR point cloud distribution.

point in the target scan not exceeding 25 cms over the total number of points in the pair of scans. In the case of registration of multiple scans, overlap is measured similarly by counting the number of corresponding points in every pair-wise scan combination within a plot not exceeding 25 cms over the total number of points in the plot.

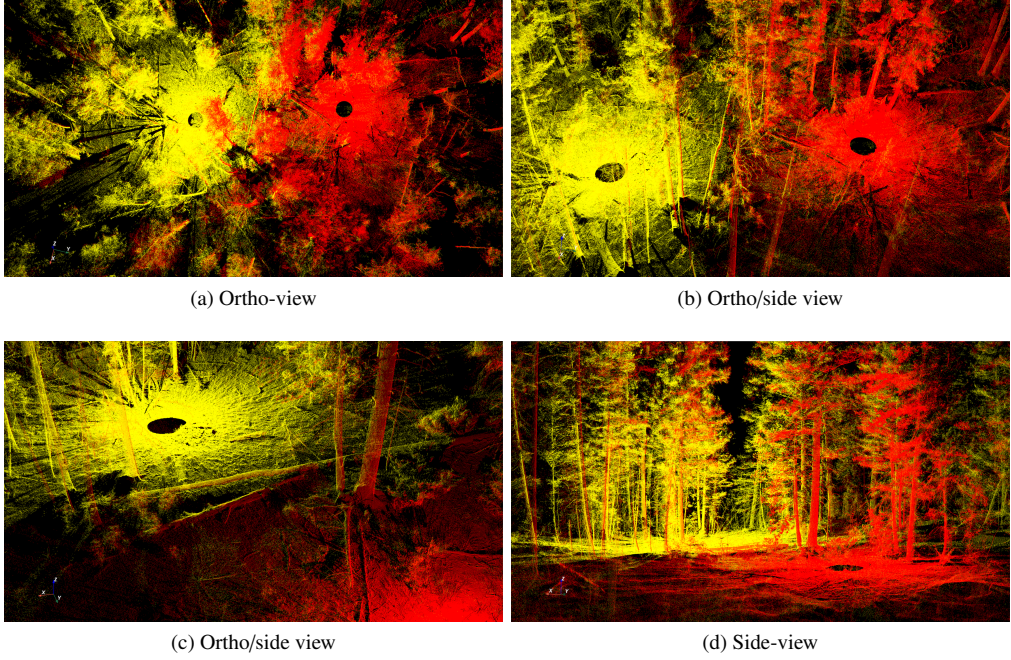


Figure 5: Pairwise alignment result of TLS based point clouds

#### 4.2. Pair-wise TLS registration

The pair-wise registration method described in Section 3.1 was evaluated on pairs of multi-view TLS point clouds. Example results are shown in Fig. 5 illustrating four views of the registration of two color-coded scans 15 x 5 meters apart on a forest site including white fir, limber pine, aspen, and Douglas fir and surface bark, trunk and bushes. Fig. 5 shows well aligned point clouds and object consistency in between scan color transitions.

*Non-uniform ground terrain:* In forest environments there are challenging scenarios that could complicate registration. One example of these is the presence of steep ground terrain. The amount of overlap between pairs of scans

in steep terrain is expected to be more sensitive to range than in more leveled terrain. Figure 4.(a-b) which shows the distribution of points as a function of range illustrates this; the tails of the distribution in the steep case are less heavy than in the nearly flat terrain. We include some additional experiments to test whether our multi-structural level approach was capable of registering under these more challenging case scenarios. Fig. 6.(a-b) gives two representative examples of the alignments produced by the proposed method with pairs of scans 10 m and 15 x 5 m apart, respectively. Both are from a plot including white fir, limber pine, aspen, Douglas fir, ponderosa pine trees. The method aligns the two point clouds consistently throughout the entire scene despite the smaller overlap compared to the near flat terrain.

To test the overall performance of the proposed approach in a diverse set of forest conditions we performed pairwise registrations in 21 distinct inventory plots for a total of 84 distinct pair scans. Each scan was originally in its ego-reference coordinate system and the registration approach was thus initialized to those ego-referenced parameters. Here, we refer to an ego-reference to measurements performed in the local "raw" sensor coordinate system. Each scan pair was physically separated by a translation distance of 15x5 m and a randomly oriented scan axis. The registration RMSE computed over all scan pairs including the plot center scan is summarized in Table 1. The results in this table show that the method is flexible and robust to operate under vegetation diversity.

Table 1: Registration RMSE.

Orientation (Degrees)			Position (meters)		
$\theta_{\text{roll}}$	$\theta_{\text{pitch}}$	$\theta_{\text{yaw}}$	$t_x$	$t_y$	$t_z$
0.08	0.04	0.09	0.014	0.016	0.0011

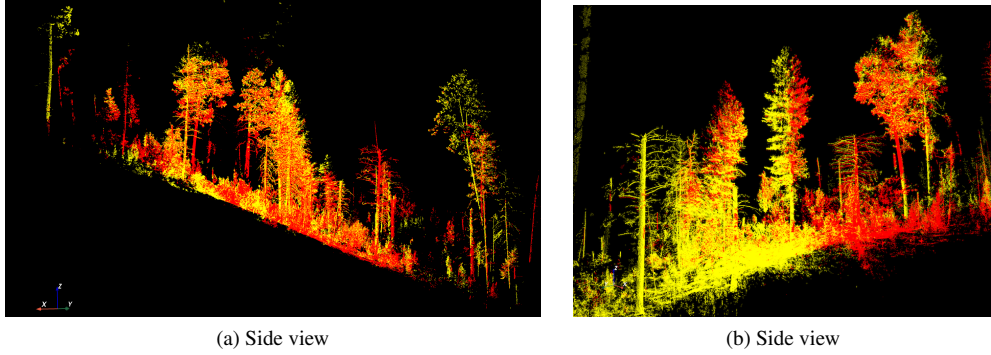


Figure 6: Pairwise TLS alignment in steep terrain.

*Overlap:* Table 2 summarizes experiments that evaluate registration performance as a function of % overlap. A total of 100 registration tests per % overlap were performed where we randomly initialize the 6 DOF alignment parameters according to a uniform distribution centered at the true alignment and that deviates by  $\pm 45^\circ$  and  $\pm 15$  m in rotation and translation, respectively. The small RMSE values across overlap reflect the effectiveness of our approach

Table 2: Registration RMSE versus % overlap.

Overlap	Orientation (Degrees)			Position (meters)		
	$\theta_{\text{roll}}$	$\theta_{\text{pitch}}$	$\theta_{\text{yaw}}$	$t_x$	$t_y$	$t_z$
$\sim 28\%$	0.039	0.036	0.034	0.013	0.019	0.011
$\sim 15\%$	0.029	0.038	0.032	0.015	0.014	0.015
$\sim 5\%$	0.037	0.036	0.045	0.010	0.015	0.013
$\sim 1\%$	0.038	0.053	0.051	0.011	0.018	0.011

and demonstrates its robustness even in cases of small overlap.

*Ecosystems without trees.* Here, we add a few additional evaluations against co-registration performance in cases where ecosystem does not contain trees. This, with the intention to show the methods' capability to exploit not only structural similarities between objects above ground surface but also from the surface topography itself. The structure in these datasets is in this case provided by hilly terrain in Ecuador. Fig.7 shows a representative example with pairs of point clouds each color coded uniformly with  $\approx 5\%$  overlap and with 0.0145 m inlier RMSE. Note that the method is effective in aligning point clouds exploiting only features from topography in as long as there is information in the scene constraining all degrees of freedom in 3D.

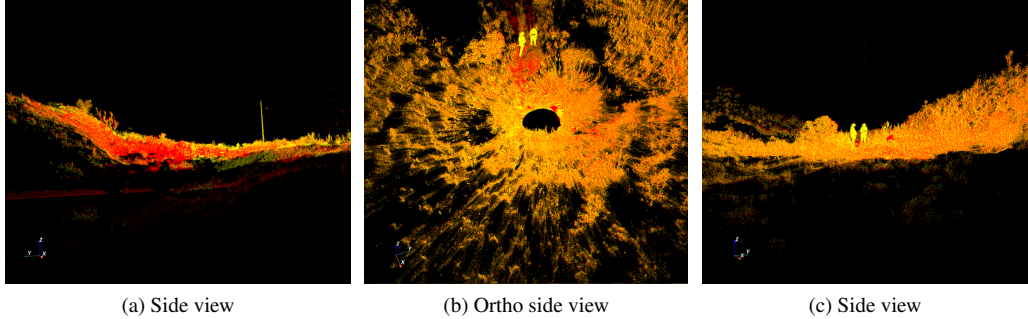


Figure 7: Co-registration in ecosystems without trees.

**Benchmark Evaluations.** Here, we compare the performance of our pair-wise registration against a target based method benchmark using Styrofoam spheres. In this comparison, the TLS scans from the dataset in [49] were co-registered using our approach and compared against the target-based method for which registration parameters were already available in the referenced dataset. This dataset contains scans of 17 plots, each with 4 scans per plot placed in a triangular pattern (one in the center and the remaining three at each corner 15 m apart from the center) and 9 targets manually placed within the scene. Note that this target based method results in alignments implicitly validated as ground truth. In Table 3, we summarize the RMSE for all pairs of scans relative to its center scan for all plots. Note that RMSE is computed relative to the registration parameters of the target based method. From Table 3 we

Table 3: Registration RMSE relative to benchmark target based method

Orientation (Degrees)			Position (meters)		
$\theta_{\text{roll}}$	$\theta_{\text{pitch}}$	$\theta_{\text{yaw}}$	$t_x$	$t_y$	$t_z$
0.058	0.065	0.032	0.016	0.012	0.007

find that our proposed framework is able to attain the accuracies of target based methods that often yield close to perfect performance. This validates that our proposed method performs as good as target based methods without the drawback of any manually placed target requirements nor detection of semantic objects in the scene while also having full automatic capabilities.

Additional experiments were conducted comparing the performance of co-registration methods alternating between minimizing a similarity function and finding correspondences between LiDAR point returns instead of human engineered or learned features suitable to urban scenarios. As these methods do not rely on lines, contours, planes, normals, edges typical to urban scenarios we deemed them more relevant to the problem at hand. The methods we compared against are the standard iterative closest point [20], coherent point drift [50], gaussian mixture models [51], support vector registration [52] and the more recent trees of gaussian mixtures [53], filterReg [54] and Bayesian coherent point drift [55]. All of these approaches have been implemented and available in the Probreg Python package [56]. For this comparison, twenty pairs of point clouds were selected at random from the available Forest plots and tested each pair for 100 trials with random initializations from the true co-registration parameters deviating by 30 degrees and 15m at one standard deviation. RMSE relative to the six degrees of freedom was then computed and summarized in table 4. Table 4 demonstrates the superiority of our method in registering scenes from heterogeneous Forest scenes

Table 4: Methods comparison of co-Registration performance by RMSE

Approach	Orientation (Degrees)			Position (meters)		
	$\theta_{\text{roll}}$	$\theta_{\text{pitch}}$	$\theta_{\text{yaw}}$	$t_x$	$t_y$	$t_z$
icp [20]	2.324	0.627	25.488	0.88	10.104	0.979
cpd [50]	0.0374	5.3638	29.8273	4.5839	10.0638	0.7630
gmm [51]	0.136	0.0398	18.311	4.583	10.063	0.763
svr [52]	1.724	3.781	23.909	5.388	9.166	0.478
gmmtree [53]	1.590	3.952	28.412	4.6770	8.501	0.618
filterReg [54]	0.512	6.764	30.691	4.451	12.503	0.903
bcpd [55]	0.2248	5.062	21.402	3.2667	12.6039	2.4279
ours	0.0224	0.0002	0.0059	0.0156	0.0149	0.0180

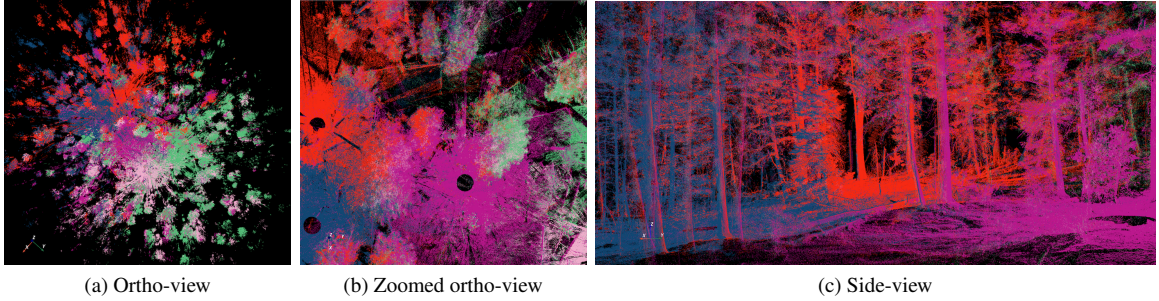


Figure 8: Multi-view alignment of TLS based point clouds

to the compared methods. This Table also, shows that some of the standard methods in the literature have issues in automatically registering scans from complex heterogeneous forests.

#### 4.3. Multi-view TLS registration

In multi-view registration, multiple scans viewing the scene from different perspectives are registered in a consistent common coordinate system. In our experiments, we typically choose the center most scan within a forest inventory plot as the reference common coordinate system, as it has the greatest domain commonality. The single scans in each of the quadrants are first registered in a pair-wise manner relative to the center scan and using the proposed multilevel approach. Projection of the aligned scans into the coordinate system of the center scan results in a stitched/accumulated set of scans that were subsequently refined using the proposed bundle refinement approach described in Section 3.2. We find experimentally, that using the paths for each scan  $i$   $\mathbf{c}_i \rightarrow \mathbf{c}_0 \rightarrow \mathbf{c}_j \forall j \notin \{i, 0\}$  and the path in the outer loop of  $\mathbf{c}_0$  without its inclusion (e.g., for  $i = 1$  the path  $\mathbf{c}_1 \rightarrow \mathbf{c}_2 \rightarrow \mathbf{c}_4 \rightarrow \mathbf{c}_3$  in Figure 3) is sufficient for the simultaneous refinement of all the scans within a forest inventory plot. This amounts to a total of 4 paths per scan  $\mathbf{c}_i$  when 5 scans are collected for each inventory plot. Figure 8 is an example that shows views of five aligned scans of a plot with each scan color coded differently. Note that there is a consistent transition between the points of aligned scans throughout the entire scene.

Quantitative performance of our refinement procedure was tested by comparing the point RMSE overall scans in a plot with and without the refinement procedure (only using multi-level registration). A total of 10 plots were tested and the point RMSE is used as the metric of performance. Here, point RMSE is computed over points in the source having at least a correspondence point in the target scan not exceeding 25 cms. Subsequently, a search over the set of corresponding points is performed and the closest target-to-source is chosen. Table 5 summarizes the results. Note that the point RMSE with the additional refinement step gets smaller, thus providing evidence that cycle consistency constraints can improve registration results in forestry multi-view TLS.

Table 5: Point RMSE refinement comparison

Without refinement	With refinement
0.087 (m)	0.0545 (m)

#### 4.4. TLS to ALS registration

Validation of our pair-wise multi-level approach was also performed on TLS and ALS registration. In this case, we used the refined set of stitched/accumulated multi-view scans from TLS within an inventory plot along with a cropped to 50x50 m point cloud from ALS centered at the (approximate) GPS location of the center TLS scan (used only for ALS region cropping). A total of 10 TLS plots were registered against ALS where the 6 DOF for alignment were randomly initialized following a random uniform distribution centered at the GPS position of the center scan and deviating by  $\pm 15$ m and  $\pm 45^\circ$  in the translation and rotation parameters, respectively. A representative example is shown in Fig. 9. The point cloud color coded in red corresponds to the cropped ALS scan while that in green is from the refined multi-view TLS. Note, although both point clouds are captured at different spatial resolution scales with ALS seemingly sparser, but with full overlap, that our approach seems to align both point clouds effectively. Quantitative performance in this case is measured using registration RMSE relative to the RTX in ALS orientation as ground truth similar to as in 4.1. The RMSE values shows our proposed approach is capable of registering within

Table 6: TLS to ALS registration RMSE

Orientation (Degrees)			Position (meters)		
$\theta_{\text{roll}}$	$\theta_{\text{pitch}}$	$\theta_{\text{yaw}}$	$t_x$	$t_y$	$t_z$
0.57	0.63	0.26	0.06	0.04	0.03

small errors of ground truth. Note in this case that errors are slightly larger compared to those of only multi-view registration. Main sources we attribute these is the lower resolution of ALS at 10 pts/m<sup>2</sup> compared to that of TLS.

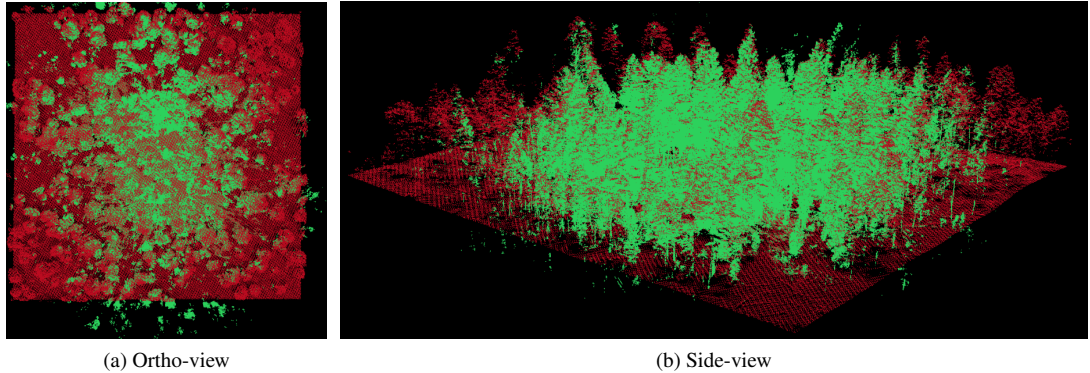


Figure 9: TLS (green) to ALS (red) alignment.

#### 4.5. pre-TLS to post-TLS fire treatment effects registration

Evaluations in this case test the capabilities of pair-wise co-registration in forest ecosystems that underwent changes by the effects of low-intensity fires targeting the ground surface. The scene before and after fire treatments are referred to as the pre and post treatment point clouds, respectively. The severity of the fire was low and the effects produced were qualitatively observable with morphologically thinning changes in the structure of surface fuels (e.g., grass, bushes). For reference, we have included in Fig.10(a-b) RGB photos of pre/post treatment effects. Results of LiDAR co-registration were included in Fig.10(c-f) where we see effective alignment of point clouds under the given

fire treatment effects. The pre treatment point cloud is color coded yellow while post is red. The resulting overall inlier RMSE was in this case of 0.014 m. Accurate alignment methods for point clouds experiencing pre/post fire or rather in the presence of scene changes in general, can be of high value to science and forest managers. They enable analysis of treatment effects over time and at high resolution spatial scales; a much needed tool for better understanding prescribed fire behavior and which can ultimately lead to improved burn plans.

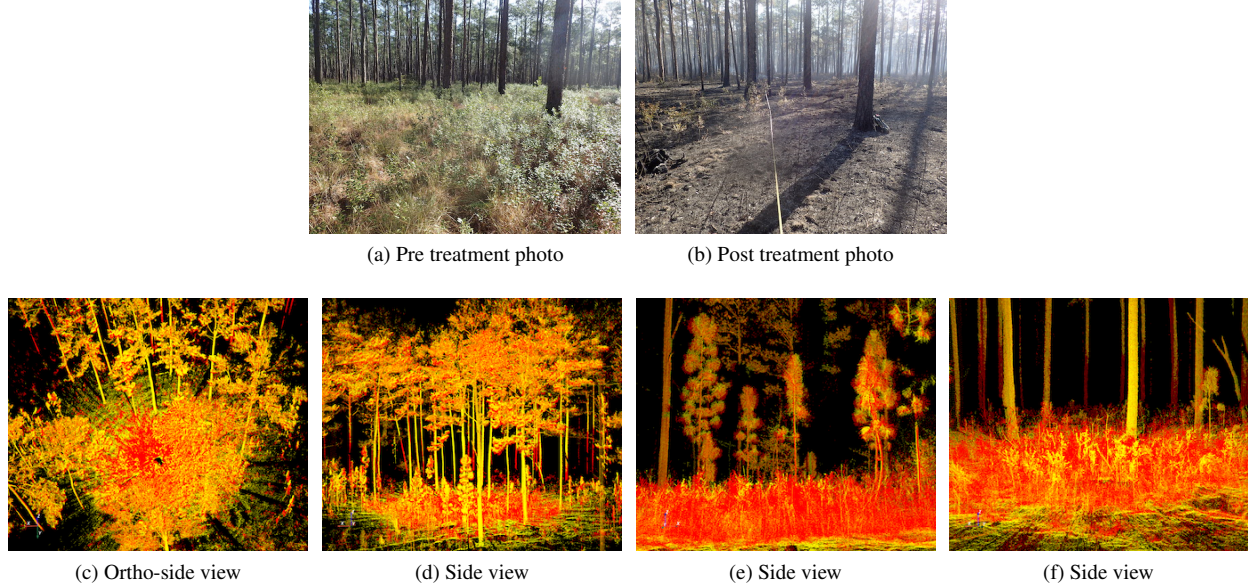


Figure 10: Pre/post treatment effects.

## 5. Conclusion

In this work, we proposed an automatic targetless multi-level approach to register pair-wise multi-view TLS LiDAR scans and ALS scans to a common reference coordinate system in complex heterogeneous forests. The resulting alignments were further refined using a bundle refinement procedure which promotes cycle consistency between the point clouds to further refine their alignments into a consistent global coordinate system. The qualitative and quantitative results of our experimentation validate that the proposed approach is both efficient and effective in aligning LiDAR scans in forestry at performances comparable with target based methods. It, in addition, showed to be robust in a variety of cases including a diverse set of resolution scales, view-points, overlap, forest heterogeneity (e.g., shrubs below the canopy, different size trees, steepness of the ground surface), low-intensity fire effects and random alignment initializations.

## Acknowledgement

Research presented in this article was supported by the Laboratory Directed Research and Development program of Los Alamos National Laboratory under project number 20220024DR.

## References

- [1] U. FAO, The state of the world's forests 2020, in: *Forests, biodiversity and people*, Rome, Italy, 2020, p. 214. doi:<https://doi.org/10.4060/ca8642en>.
- [2] J. C. White, N. C. Coops, M. A. Wulder, M. Vastaranta, T. Hilker, P. Tompalski, Remote sensing technologies for enhancing forest inventories: A review, *Canadian Journal of Remote Sensing* 42 (5) (2016) 619–641.
- [3] A. Atchley, J. A. Linn, Rodman, C. Hoffman, J. D. Hyman, F. Pimont, C. Sieg, R. S. Middleton, Effects of fuel spatial distribution on wildland fire behaviour, *International Journal of Wildland Fire* 30 (3) (2021) 179–189.

[4] E. Tomppo, T. Gschwantner, M. Lawrence, R. E. McRoberts, K. Gabler, K. Schadauer, C. Vidal, A. Lanz, G. Ståhl, E. Cienciala, National forest inventories, Pathways for Common Reporting, European Science Foundation 1 (2010) 541–553.

[5] R. O. Dubayah, J. B. Drake, Lidar remote sensing for forestry, *Journal of forestry* 98 (6) (2000) 44–46.

[6] J. Hyppä, X. Yu, H. Hyppä, M. Vastaranta, M. Holopainen, A. Kukko, H. Kaartinen, A. Jaakkola, M. Vaaja, J. Koskinen, et al., Advances in forest inventory using airborne laser scanning, *Remote sensing* 4 (5) (2012) 1190–1207.

[7] T. Hilker, M. van Leeuwen, N. C. Coops, M. A. Wulder, G. J. Newnham, D. L. Jupp, D. S. Culvenor, Comparing canopy metrics derived from terrestrial and airborne laser scanning in a douglas-fir dominated forest stand, *Trees* 24 (5) (2010) 819–832.

[8] M. Holopainen, V. Kankare, M. Vastaranta, X. Liang, Y. Lin, M. Vaaja, X. Yu, J. Hyppä, H. Hyppä, H. Kaartinen, et al., Tree mapping using airborne, terrestrial and mobile laser scanning—a case study in a heterogeneous urban forest, *Urban forestry & urban greening* 12 (4) (2013) 546–553.

[9] T. Hilker, N. C. Coops, D. S. Culvenor, G. Newnham, M. A. Wulder, C. W. Bater, A. Siggins, A simple technique for co-registration of terrestrial lidar observations for forestry applications, *Remote sensing letters* 3 (3) (2012) 239–247.

[10] V. Kankare, J. Vauhkonen, T. Tanhuanpää, M. Holopainen, M. Vastaranta, M. Joensuu, A. Krooks, J. Hyppä, H. Hyppä, P. Alho, et al., Accuracy in estimation of timber assortments and stem distribution—a comparison of airborne and terrestrial laser scanning techniques, *ISPRS Journal of Photogrammetry and Remote Sensing* 97 (2014) 89–97.

[11] S. Bauwens, H. Bartholomeus, K. Calders, P. Lejeune, Forest inventory with terrestrial lidar: A comparison of static and hand-held mobile laser scanning, *Forests* 7 (6) (2016) 127.

[12] X. Ge, Q. Zhu, Target-based automated matching of multiple terrestrial laser scans for complex forest scenes, *ISPRS Journal of Photogrammetry and Remote Sensing* 179 (2021) 1–13.

[13] A. Bienert, H.-G. Maas, Methods for the automatic geometric registration of terrestrial laser scanner point clouds in forest stands, in: *Proceedings of the ISPRS Workshop on Laser Scanning*, Societe Francaise de Photogrammetrie et de Teledetection Lemmer, 2009, pp. 1–2.

[14] D. Kelbe, J. Van Aardt, P. Romanczyk, M. Van Leeuwen, K. Cawse-Nicholson, Marker-free registration of forest terrestrial laser scanner data pairs with embedded confidence metrics, *IEEE transactions on geoscience and remote sensing* 54 (7) (2016) 4314–4330.

[15] J. Liu, X. Liang, J. Hyppä, X. Yu, M. Lehtomäki, J. Pyörälä, L. Zhu, Y. Wang, R. Chen, Automated matching of multiple terrestrial laser scans for stem mapping without the use of artificial references, *International journal of applied earth observation and geoinformation* 56 (2017) 13–23.

[16] J.-F. Tremblay, M. Béland, Towards operational marker-free registration of terrestrial lidar data in forests, *ISPRS Journal of Photogrammetry and Remote Sensing* 146 (2018) 430–435.

[17] P. Polewski, W. Yao, L. Cao, S. Gao, Marker-free coregistration of uav and backpack lidar point clouds in forested areas, *ISPRS Journal of Photogrammetry and Remote Sensing* 147 (2019) 307–318.

[18] X. Ge, Q. Zhu, L. Huang, S. Li, S. Li, Global registration of multiview unordered forest point clouds guided by common subgraphs, *IEEE Transactions on Geoscience and Remote Sensing* 60 (2021) 1–14.

[19] X. Liang, A. Kukko, H. Kaartinen, J. Hyppä, X. Yu, A. Jaakkola, Y. Wang, Possibilities of a personal laser scanning system for forest mapping and ecosystem services, *Sensors* 14 (1) (2014) 1228–1248.

[20] P. J. Besl, N. D. McKay, A method for registration of 3-d shapes, *IEEE Transactions on Pattern Analysis and Machine Intelligence* 14 (2) (1992) 239–256. doi:10.1109/34.121791.

[21] Y. Chen, G. Medioni, Object modelling by registration of multiple range images, *Image and vision computing* 10 (3) (1992) 145–155.

[22] D. Aiger, N. J. Mitra, D. Cohen-Or, 4pointss congruent sets for robust pairwise surface registration, *ACM Trans. Graph.* 27 (3) (2008) 85:1–85:10. doi:10.1145/1360612.1360684  
URL <http://doi.acm.org/10.1145/1360612.1360684>

[23] R. B. Rusu, N. Blodow, M. Beetz, Fast point feature histograms (fpfh) for 3d registration, in: *2009 IEEE International Conference on Robotics and Automation*, 2009, pp. 3212–3217. doi:10.1109/ROBOT.2009.5152473.

[24] Y. Li, G. Wang, X. Ji, Y. Xiang, D. Fox, Deepim: Deep iterative matching for 6d pose estimation, in: *Proceedings of the European Conference on Computer Vision (ECCV)*, 2018, pp. 683–698.

[25] W. Lu, G. Wan, Y. Zhou, X. Fu, P. Yuan, S. Song, Deepvcp: An end-to-end deep neural network for point cloud registration, in: *Proceedings of the IEEE/CVF International Conference on Computer Vision*, 2019, pp. 12–21.

[26] C. Brenner, C. Dold, N. Ripperda, Coarse orientation of terrestrial laser scans in urban environments, *ISPRS journal of photogrammetry and remote sensing* 63 (1) (2008) 4–18.

[27] T. Sumi, S. Kanai, et al., Multiple tls point cloud registration based on point projection images., *International Archives of the Photogrammetry, Remote Sensing & Spatial Information Sciences* 42 (2) (2018).

[28] B. Xiong, D. Li, Z. Zhou, F. Li, Fast registration of terrestrial lidar point clouds based on gaussian-weighting projected image matching, *Remote Sensing* 14 (6) (2022) 1466.

[29] X. Xu, P. Wang, X. Gan, J. Sun, Y. Li, L. Zhang, Q. Zhang, M. Zhou, Y. Zhao, X. Li, Automatic marker-free registration of single tree point-cloud data based on rotating projection, *Artificial Intelligence in Agriculture* 6 (2022) 176–188.

[30] M. Kedzierski, A. Fryskowska, Terrestrial and aerial laser scanning data integration using wavelet analysis for the purpose of 3d building modeling, *Sensors* 14 (7) (2014) 12070–12092.

[31] T.-A. Teo, S.-H. Huang, Surface-based registration of airborne and terrestrial mobile lidar point clouds, *Remote Sensing* 6 (12) (2014) 12686–12707.

[32] H. Wu, M. Scaioni, H. Li, N. Li, M. Lu, C. Liu, Feature-constrained registration of building point clouds acquired by terrestrial and airborne laser scanners, *Journal of Applied Remote Sensing* 8 (1) (2014) 083587–083587.

[33] B. Yang, Y. Zang, Z. Dong, R. Huang, An automated method to register airborne and terrestrial laser scanning point clouds, *ISPRS Journal of Photogrammetry and Remote Sensing* 109 (2015) 62–76.

[34] X. Cheng, X. Cheng, Q. Li, L. Ma, Automatic registration of terrestrial and airborne point clouds using building outline features, *IEEE Journal of Selected Topics in Applied Earth Observations and Remote Sensing* 11 (2) (2018) 628–638.

[35] X. Ling, R. Qin, A graph-matching approach for cross-view registration of over-view and street-view based point clouds, *ISPRS Journal of*

Photogrammetry and Remote Sensing 185 (2022) 2–15.

- [36] H. Guan, Y. Su, T. Hu, R. Wang, Q. Ma, Q. Yang, X. Sun, Y. Li, S. Jin, J. Zhang, et al., A novel framework to automatically fuse multiplatform lidar data in forest environments based on tree locations, *IEEE Transactions on Geoscience and Remote Sensing* 58 (3) (2019) 2165–2177.
- [37] W. Dai, B. Yang, X. Liang, Z. Dong, R. Huang, Y. Wang, J. Pyörälä, A. Kukko, Fast registration of forest terrestrial laser scans using key points detected from crowns and stems, *International Journal of Digital Earth* 13 (12) (2020) 1585–1603.
- [38] X. Wang, Z. Yang, X. Cheng, J. Stoter, W. Xu, Z. Wu, L. Nan, Efficient registration of forest point clouds by global matching of relative stem positions, *arXiv preprint arXiv:2112.11121* (2021).
- [39] C. E. Shannon, A mathematical theory of communication, *The Bell system technical journal* 27 (3) (1948) 379–423.
- [40] G. Pandey, J. R. McBride, S. Savarese, R. M. Eustice, Automatic targetless extrinsic calibration of a 3d lidar and camera by maximizing mutual information, in: *Twenty-Sixth AAAI Conference on Artificial Intelligence*, 2012.
- [41] J. Castorena, C. Creusere, D. Voelz, Using finite moment rate of innovation for lidar waveform complexity estimation, in: *2010 Conference Record of the Forty Fourth Asilomar Conference on Signals, Systems and Computers*, IEEE, 2010, pp. 608–612.
- [42] J. Castorena, C. D. Creusere, D. Voelz, Modeling lidar scene sparsity using compressive sensing, in: *2010 IEEE International Geoscience and Remote Sensing Symposium*, IEEE, 2010, pp. 2186–2189.
- [43] M. A. Fischler, R. C. Bolles, Random sample consensus: a paradigm for model fitting with applications to image analysis and automated cartography, *Communications of the ACM* 24 (6) (1981) 381–395.
- [44] J. Castorena, G. V. Puskorius, G. Pandey, Motion guided lidar-camera self-calibration and accelerated depth upsampling for autonomous vehicles, *Journal of Intelligent & Robotic Systems* 100 (3) (2020) 1129–1138.
- [45] D. P. Bertsekas, The auction algorithm: A distributed relaxation method for the assignment problem, *Annals of operations research* 14 (1) (1988) 105–123.
- [46] M. Moakher, Means and averaging in the group of rotations, *SIAM Journal on Matrix Analysis and Applications* 24(1) (2002) 597–621.
- [47] R. Hartley, K. Aftab, J. Trumpf, L1 rotation averaging using the weiszfeld algorithm, in: *CVPR 2011*, 2011, pp. 3041–3048. doi:10.1109/CVPR.2011.5995745.
- [48] Q.-Y. Zhou, J. Park, V. Koltun, Open3D: A modern library for 3D data processing, *arXiv:1801.09847* (2018).
- [49] C. Gollob, T. Ritter, A. Nothdurft, Comparison of 3d point clouds obtained by terrestrial laser scanning and personal laser scanning on forest inventory sample plots, *Data* 5 (4) (2020) 103.
- [50] A. Myronenko, X. Song, Point set registration: Coherent point drift, *IEEE transactions on pattern analysis and machine intelligence* 32 (12) (2010) 2262–2275.
- [51] B. Jian, B. C. Vemuri, Robust point set registration using gaussian mixture models, *IEEE transactions on pattern analysis and machine intelligence* 33 (8) (2010) 1633–1645.
- [52] D. Campbell, L. Petersson, An adaptive data representation for robust point-set registration and merging, in: *Proceedings of the IEEE international conference on computer vision*, 2015, pp. 4292–4300.
- [53] B. Eckart, K. Kim, J. Kautz, Fast and accurate point cloud registration using trees of gaussian mixtures, *arXiv preprint arXiv:1807.02587* (2018).
- [54] W. Gao, R. Tedrake, Filterreg: Robust and efficient probabilistic point-set registration using gaussian filter and twist parameterization, in: *Proceedings of the IEEE/CVF Conference on Computer Vision and Pattern Recognition*, 2019, pp. 11095–11104.
- [55] O. Hirose, A bayesian formulation of coherent point drift, *IEEE transactions on pattern analysis and machine intelligence* 43 (7) (2020) 2269–2286.
- [56] Kenta-Tanaka et al., probreg.  
URL <https://probreg.readthedocs.io/en/latest/>